Grid-forming and Power Tracking by Photovoltaic Systems without Battery Storage

Horst Schulte[1] and Nico Goldschmidt[1] and Moritz Andrejewski[1]

Abstract— An overall photovoltaic power plant control concept with grid-forming availability without battery storage is proposed. Grid-forming voltage-source converter control is usually studied decoupled from the primary source. Recent studies consider the voltage drop on the DC side for grid-forming control. Until now, the photovoltaic generator and DC-DC converter dynamics are not included. However, it is necessary to consider the overall system dynamics for control design with the objective of fast power control. A generalized control scheme for a two-stage photovoltaic generator model consisting of an aggregated single-diode model of the photovoltaic voltage-controlled current source and a DC-DC converter for tracking the requested power combined with a grid-forming voltage-source converter is presented. For this purpose, the classical maximum power tracking is extended by a generalized demanded tracking. The performance of the approach is evaluated using relevant test cases with active and reactive power requests, grid events like grid voltage drop, phase angle step changes, and fluctuations of the primary energy resource.

I. INTRODUCTION

Due to the increasing amount of distributed energy sources and the decreasing number of bulk synchronous machines, ancillary services like fast frequency reserve must be provided, i.e., by photovoltaic (PV) power plants. It is shown in the POSYTYF report D2.2 [1] that the performance of the fast frequency reserve depends essentially on the dynamics of the primary power conversion. However, the adequate interaction between the PV generator (primary power conversion) and the feed-in by power electronic converters (secondary power conversion) must also be investigated. In addition, it is essential to examine whether it is possible to provide rapid change in instantaneous power, both as negative and positive changes, without the need for extra battery storage. As battery storage systems are expensive to install and maintain, as well as the extraction of raw materials is not climate-neutral, the operation of PV power plants without storage is an essential requirement for the design of the system, especially the control system.

In the previous work [2], the primary system from the conversion of the irradiation to the DC bus was investigated. A demanded power tracking (DPT) controller and model-based design concept for a large operating range were presented. It has been verified that an external power demand can be followed under the assumption of the available power reserve. So far, it has not been investigated how the DPT can be integrated with the voltage source inverter. In detail, the research question is addressed which advantages a grid-forming has compared to grid-following inverter in combination with power tracking control of the primary conversion. Since the eigendynamics of both subsystems are closely related, it is necessary to analyze them simultaneously. The comparison is based on test cases that evaluate both the disturbance rejection and command response dynamics of the overall control system.

The literature overview of current research reflects two areas: First, the demanded PV tracking, and second, the grid-forming control approaches, which are combined in this paper. In [3] a power reserve control technique based on PV module voltage variation is proposed. The approach is applied to offer primary frequency reserve and virtual inertia. In [4], a strategy with variable maximum power tracking controller using an artificial neural network (ANN) is proposed. The maximum available power is estimated using an ANN model first. Then, in the second step, the current source of the PV generator is controlled by a PI voltage regulator to calculate the requested power considering the estimated maximum available power. A so-called pseudo maximum power point tracking (PMPPT) is presented in [5], which makes it possible to operate PV power plants with reserve power capacity without employing a battery for storage. Control strategies for frequency support by hybrid power plants consisting of PV and rotating generators without battery energy storage have been formulated in [6]. Two deloaded operation modes of PV systems are suggested, where a cost analysis shows that the proposed concept is economical compared to battery usage for grid frequency stabilization. In [7], a model-based maximum power point tracking (MPPT) technique is presented for a two-stage (DC-DC and DC-AC units are separated from each other as it is also assumed in the present work) grid-connected photovoltaic systems, where the loci of the maximum power points are specified accurately based on the P-V map.

The precise, generally applicable definition of grid-forming (GFOM) converters in large power grids is still an open problem. Grid operators, converter manufacturers, and academic research laboratories are investigating the requirements for future systems with GFOM behavior. An attempt to define the characteristics and requirements is described in [8], [9]. It should be emphasized that different concepts for

grid-forming controls have been recently developed like the virtual synchronous machine (VISMA) based voltage-source converter (VSC) control [10], universal droop controller [11], direct voltage control [12], GFOM with current limitation algorithm [13], [14] and dual port control [15]. In this work, we investigate a droop controller concept with a lower-level current control. The performance of the grid-forming VSC is compared with a standard grid-following controller [16]. Both VSC are integrated into the power demanded control of the PV power plant.

The paper is organized as follows: In Section II the overall system description of the PV power plant with VSC and equivalent grid model is given. The following two sections explain the mathematical models, decentralized controllers, and their coordination. In Section III the reduced mathematical model and large-signal control scheme of the primary conversion in Takagi-Sugeno (TS) form is introduced. Section IV describes the reduced mathematical model of the voltage source converter and control schemes for grid-following and grid-forming. In Section V simulation studies of the following test scenarios are presented:

- Response to active power request
- Response to reactive power request
- Jump-shaped change in solar radiation
- Grid disturbance rejection

A final conclusion and references to future work are given in Section VI.

II. OVERALL SYSTEM DESCRIPTION AND CONTROL SCHEME

A. Overall System Description

The generic two-stage grid-connected photovoltaic (PV) systems separated into a primary and secondary power conversion are shown in Figure 1. The primary power conversion unit contains the PV generator to convert solar radiation into electrical DC power and the DC-DC converter for maximum power point or demanded power tracking. System inputs of the PV generator are the irradiation S and the controllable voltage v_{pv}. The primary converter injects power into the
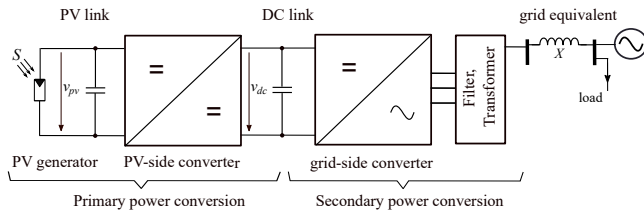

Fig. 1. Two-stage grid integrated PV power plant

secondary power conversion over the DC link. To convert the DC voltage into a three-phase AC voltage, an inverter with an LCL filter and a transformer connected to the grid is used. Note that the generic primary power conversion is related to a central tracker at the array level since we do not

study partial shading in the system analysis where distributed DC-DC converters (e.g., at string level) are aggregated to a central converter. The secondary power conversion (see Figure 1) from the DC bus to the AC grid is generated by a voltage source converter. The VSC is controlled either as a current source in grid-following mode or as a voltage source in grid-forming mode. The hardware and circuit topology are not changed at all.

B. Overall Control Scheme

The primary and secondary power conversions illustrated in Figure 2 are automatically regulated by three decentralized control loops. The inner voltage controller (first control loop) and the PV power tracking controller (second control loop) are related to the primary power conversion. The third control loop contains the grid-forming control of the inverter, which is referred to here as secondary power conversion.

For voltage control in the first loop, the current i_L through the inductance and voltage v_c at the capacitor of the DC-DC converter are measured, where $v_c = v_{pv}$, see Figure 3. To track the PV voltage v_{pv}, the duty cycle d of the DC-DC converter is set. Details are described in Section III-C.
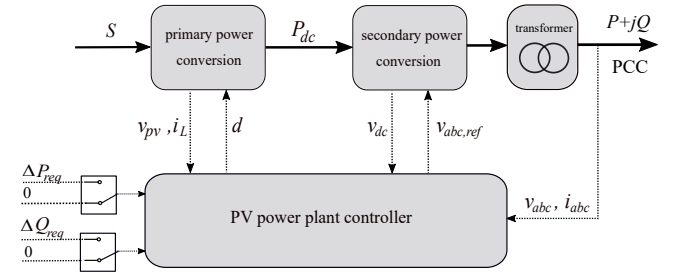

Fig. 2. Overall Control Scheme of grid integrated PV power plant

To regulate the power injection of the voltage source converter the three-phase voltages v_{abc} and currents i_{abc} are measured at the PCC. The control variable is the space vector $\underline{E}$ with amplitude E and phase ϕ, which is converted into a three-phase reference value $v_{abc,ref}$ with the fundamental frequency ω. In Section IV-B, a grid-forming controller is presented in detail with an inner-loop current control for current limitation and voltage vector generation. The overall control objective is to either extract the maximum possible power from the PV power plant or to follow a reference power signal, taking into account the achievable limits of the resource. The desired behavior is represented by two modes:

- *MPPT mode*: Generation of the maximum possible electrical power, no power request: $\Delta P_{req} \neq 0$ and $\Delta Q_{req} \neq 0$
- *DPT mode*: Follow, if possible the power request $\Delta P_{req} \neq 0$ and $\Delta Q_{req} \neq 0$

The switches in Figure 2 illustrate the selection options for external activation of these two power plant modes.

III. Modeling and Control of Primary Power Conversion Unit

This section briefly introduces the models and control system of the primary conversion, i.e. the PV generator model and the DC-DC converter with voltage control and demanded power tracking. Details of the control laws, in particular the LMI-based controller synthesis for large-signal input-to-state stability (ISS) analysis, are described in [2].

A. PV-Generator

The mathematical model of the PV generator results from the aggregation of all PV modules and single cells of a module where the current and voltage are suitably multiplied. The equivalent circuit has N_p cells in parallel and N_s in series with an effective shunt resistor $(N_s/N_p)R_h$ and a current source $N_p i_{ph}$ with i_{ph} as the light current of a single cell. The irradiation S with the physical unit W/m^2 is related to the direct (normal to the PV cell array) and the diffuse irradiation. By applying Kirchhoff's laws, we obtain the aggregated PV generator model $i_{pv} = f_{pv}(v_{pv}, S, T_c)$ as the terminal voltage controlled, denoted as v_{pv}, current source that depends on the cell temperature T_c and irradiation S

$$i_{pv} = N_p i_{ph}(S, T_c) - N_p i_s(S, T_c)\left[e^{\frac{v_{pv}}{N_s v_{T,STC} A_n}} - 1\right] - \frac{N_p}{N_s}\frac{v_{pv}}{R_h},$$
(1)

with light current of a single cell

$$i_{ph} = \frac{S}{S_{STC}} i_{ph,sc,STC}\left(1 + \alpha_T\left(T_c - T_{c,STC}\right)\right),$$
(2)

and with the saturation current of the diode's diffusion effect

$$i_s = \frac{i_{ph} - \frac{v_{oc}}{R_h}}{e^{\frac{v_{oc}}{A_n v_{T,STC}}} - 1}$$
(3)

and with v_{oc} as open-circuit voltage of the diode model

$$v_{oc} = v_{oc,STC}\left(1 + \beta_T\left(T_c - T_{c,STC}\right)\right),$$
(4)

where $v_{T,STC} = 25.7$ mV denotes the thermal voltage of p-n junction at standard test conditions (STC). The others parameters are the shunt resistor R_h to model the cell losses, k as the Boltzmann constant with $k = 1.381 \times 10^{-23}$ J/K, A_n as the constant ideality factor and the elementary charge $q = 1.602 \times 10^{-19}$ As. The temperature-dependent models (2) and (4) contain $\alpha_T > 0$ and $\beta_T < 0$ as temperature coefficients and $T_{c,STC} = 298°$K as the temperature at STC.

B. DC-DC Converter with voltage controlled current source

The model for the design of the primary power conversion controller (see Figure 1 and Figure 2) consists of the state-space average model of a switched DC-DC buck converter combined with the static model (1) of the current source $i_{pv} = f_{pv}(v_{pv}, S, T_c)$. The corresponding equivalent circuit diagram is shown in Figure 3. In contrast to the standard application of DC-DC converters, in PV systems, the input voltage v_{pv} is set about a constant DC bus voltage v_{dc} utilizing a duty cycle.
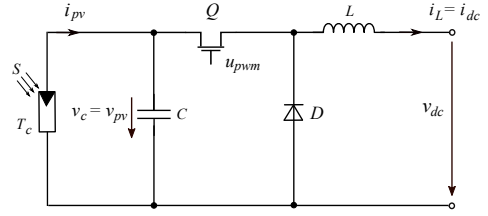

Fig. 3. PV generator as voltage input of DC-DC buck converter

.

Based on the assumption that the PWM switching frequency $f_{fw} = 1/T_{fw}$ is larger compared to the LC circuit dynamics the duty cycle d is given by the average value

$$d = \frac{1}{T_{sw}} \int_0^{T_{sw}} u_{pwm}(t)dt = \frac{T_{on}}{T_{sw}},$$
(5)

where T_{on} denotes the duration of the switched-on pulse signal. The state-space average model related to Figure 3 is given as follows

$$\dot{x}_1 = -\frac{1}{C}x_2 u_1 + \frac{1}{C}f_{pv}(x_1, S, T_c),$$
$$\dot{x}_2 = \frac{1}{L}x_1 u_1 - \frac{1}{L}u_2,$$
(6)

with i_L as current through the switched inductance and the state vector $\mathbf{x} := (x_1, x_2)^T = (v_{pv}, i_L)^T$, where $v_{pv} = v_c$ (see Figure 3) and $\mathbf{u} := (u_1, u_2)^T = (d, v_{dc})^T$. The state-space model for the following optimal controller design is based on a weighted combination of locally valid linear state-space models. These are calculated by Taylor linearization of (6) around selected equilibrium points $i = 1, \ldots, N_r$. The procedure is i.e. briefly described in [17]. From this follows the i'th linear model

$$\Delta \dot{\mathbf{x}}_i = \underbrace{\begin{pmatrix} -\frac{1}{C}\frac{\partial f_{pv}(x_1^e, S^e, T_c^e)}{\partial x_1} & -\frac{u_1^e}{C} \\ \frac{u_1^e}{L} & 0 \end{pmatrix}}_{\mathbf{A}_i} \Delta \mathbf{x}_i + \underbrace{\begin{pmatrix} -\frac{x_2^e}{C} & 0 \\ \frac{x_1^e}{L} & -\frac{1}{L} \end{pmatrix}}_{\mathbf{B}_i} \Delta \mathbf{u}_i$$
(7)

with the states $\mathbf{x}_i^e = (x_{1,i}^e, x_{2,i}^e)^T$ and inputs $\mathbf{u}_i = (u_{1,i}^e, u_{2,i}^e)^T$ at the i'th equilibrium point, related environmental conditions S_i^e and $T_{c,i}^e$ and the distance $\Delta \mathbf{x}_i = \mathbf{x}_i - \mathbf{x}_i^e$, $\Delta \mathbf{u}_i = \mathbf{u}_i - \mathbf{u}_i^e$ to the i'th equilibrium point. Calculation of the equilibrium points is done in a straightforward way by:

1) Selection of an arbitrary PV voltage values within $v_{pv} \in [V_{dc}, v_{oc}]$, where

$$x_{1,i}^e = v_{pv,i}$$
(8)

assuming that the DC voltage at the output of the buck converter is constant $V_{dc} \equiv$ const.

2) Calculation of the related operating point of the input

$$u_{1,i}^e = d_i^e = \frac{V_{dc}}{x_{1,i}^e} \quad \text{and} \quad u_{2,i}^e = V_{dc} \quad \forall i,$$
(9)

which results in $\Delta u_{2,i} = V_{dc} - u_{2,i}^e = 0$

3) Calculation of current i_L at the equilibrium point

$$x_{2,i}^e = i_L^e = \underbrace{f_{pv}(x_{1,i}^e, S_i^e, T_{c,i}^e)}_{i_{pv}} \frac{1}{d_i^e} \qquad (10)$$

for specified irradiation S_i^e and cell temperature $T_{c,i}^e$.

Hence, the steady-state operating points $\{\mathbf{u}_i^e, \mathbf{x}_i^e\}$ of (11) are defined by the terminal voltage at the PV generator, aggregated irradiation, and cell temperature. Due to the DC voltage in the DC bus v_{dc}, which is assumed to be almost constant the control-oriented local models have a single input $\Delta u_i := \Delta u_{1,i} = u_1 - u_{1,i}^e$ with $u_i := u_{1,i}$ and $u := u_1$.

$$\Delta \dot{\mathbf{x}}_i = \underbrace{\begin{pmatrix} -\frac{1}{C} \frac{\partial f_{pv}(x_1^e, S^e, T_c^e)}{\partial x_1} & -\frac{u_1^e}{C} \\ \frac{u_1^e}{L} & 0 \end{pmatrix}}_{\mathbf{A}_i} \Delta \mathbf{x}_i + \underbrace{\begin{pmatrix} -\frac{x_2^e}{C} \\ \frac{x_1^e}{L} \end{pmatrix}}_{\mathbf{b}_i} \Delta u_i . \quad (11)$$

To merge the set of linear models into a TS model with a common state vector, we rewrite (11) as

$$\dot{\mathbf{x}} = \mathbf{A}_i \mathbf{x} + \mathbf{b}_i u \underbrace{- \mathbf{A}_i \mathbf{x}_i^e - \mathbf{b}_i u_i^e}_{\mathbf{a}_i} , \qquad (12)$$

whereby the Δ-vectors in (11) are split into their absolute state vector $\mathbf{x}$, input value u and the affine part $\mathbf{a}_i$. Which allows us to sum up all linear models $i = 1, \ldots, N_r$ into a convex combination as Takagi-Sugeno state-space model

$$\dot{\mathbf{x}} = \sum_{i=1}^{N_r} h_i(\mathbf{z}) \big(\mathbf{A}_i \mathbf{x} + \mathbf{b}_i u + \mathbf{a}_i \big) , \qquad (13)$$

where $\mathbf{a}_i = -\mathbf{A}_i \mathbf{x}_i^e - \mathbf{b}_i u_i^e$ and $\mathbf{z} = (z_1, z_2, z_3)^T$ with the premise variables

$$z_1 = x_1, \qquad z_2 = S, \qquad z_3 = T_c . \qquad (14)$$

The set of sub-models $\{\mathbf{A}_i, \mathbf{b}_i, \mathbf{a}_i\}$ for $i = 1, \ldots, N_r$ with $N_r = 5 \cdot 7 \cdot 3 = 105$ is related to the selected operating points

$$\begin{aligned} v_{pv}^e = x_1^e &= \{0.9, 0.925, 0.95, 0.975, 1.0\} \cdot v_{pv,MPP} , \\ S^e &= \{200, 333, 467, 600, 733, 867, 1000\} , \qquad (15) \\ T_c^e &= \{273, 298, 323\} \end{aligned}$$

where $v_{pv}^e \times S^e \times T_c^e$ with $v_{pv,MPP}$ as the voltage at the maximum power point for STC. Finally, the entire model for controller design is obtained by blending the local models by convex locally valid (> 0) membership functions $h_i(\mathbf{z})$. Related to the large-signal model (13), a PV voltage controller of the form

$$u = -\sum_{i=1}^{N_r} h_i(\mathbf{z}) \mathbf{k}_{x,i}^T (\mathbf{x} - \mathbf{x}_i^e) + \sum_{i=1}^{N_r} h_i(\mathbf{z}) k_{I,i} \int_0^t \big(v_{pv,ref} - v_{pv} \big) d\tau ,$$
$$(16)$$

where $\mathbf{x}_i^e = (v_{pv,i}^e, i_{L,i}^e)^T$ with the output equation

$$y = v_{pv} = \mathbf{c}^T \mathbf{x} = \begin{pmatrix} 1 & 0 \end{pmatrix} \mathbf{x}, \qquad y_{ref} = v_{pv,ref} . \qquad (17)$$

can be proposed. An optimum control loop design with suitable LMI region constraints [18] can be executed for the combination of the plant model (13) and controller law (16)

using convex optimization [19]. The theoretical foundation and details are presented in [2]. In this paper, we focus on the overall control and grid integration with GFOM converters. For a better understanding, the block structure of the voltage control system (first control loop of the overall system) is shown in Figure 4. The large-signal controller is based on
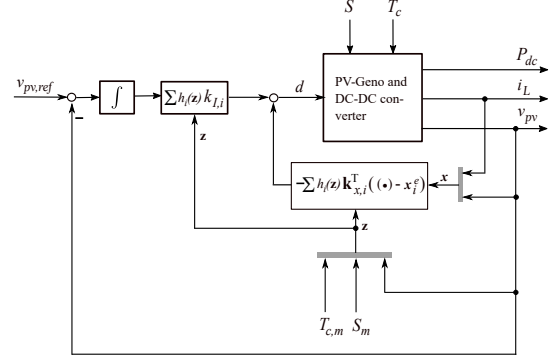

Fig. 4. Voltage controller of primary power converter

a convex time-variant combination of linear controllers xx with guaranteed global stability. Simulation results with a reference signal (step at $t = 1.0$ s and at $t = 2.5$ s) and an abrupt change in irradiation at $t = 1.05$ s and $t = 2.4$ s are shown in Figure 5. It can be seen that the command response and disturbance rejection of the Takagi-Sugeno controller (16) outperforms the linear controller (frozen controller for a constant $\mathbf{z}$) in the whole operating region. That means that the linear controller only works well in its local operating range (upper diagram of Figure 5). Due to the non-linear dynamics of the PV-generator DC-DC system (6), the linear controller loses performance the larger the distance to the operating point (see the lower diagram of Figure 5).
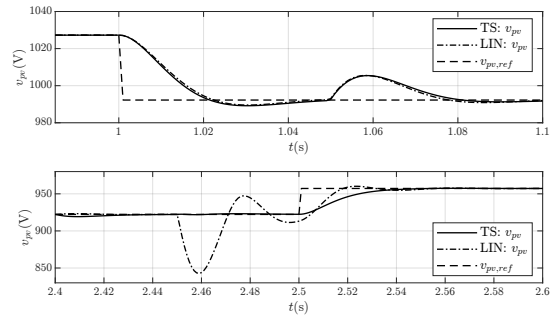

Fig. 5. Comparision between the TS controller and a linear controller

C. Demanded Power Tracking

The demanded power tracking (DPT) controller provides the set point $v_{pv,ref}$ for the lower-level voltage control to achieve operating points in a wide range covered by the so-called P-V curve. The P-V curve results from the multiplication of the PV generator model (1) with v_{pv}. The related I-V curve (1) and P-V curve for a 3.1 MW photovoltaic generator with S variation is shown in Figure 6. There are two control

techniques that can be used for power tracking: A model-free approach using extremum seeking control and a method based on the estimated P-V diagram. It has been shown that the model-based approach fulfills the requirements for the dynamics of fast frequency response for the primary side.

For a better evaluation, the power tracking behavior is shown in Figure 7 with decreasing and increasing power demand at constant irradiation and cell temperature. In the upper diagram of Figure 7 the produced PV generator is compared to the demanded reference power. Here, the non-minimum phase behavior is clearly visible. This is due to the fact that when v_{pv} is reduced by the inner-loop controller, the current i_L through the induction of the DC-DC buck converter initially increases for a short time and thus, the power in the DC link increases as well. However, the effect disappears after a short time by a further drop in PV voltage, so that the real power follows the required power after about 100 ms. To conclude, the performance of fast power-tracking are determined by the dynamics of voltage control and current rate limitation by the DC-DC converter inductance.
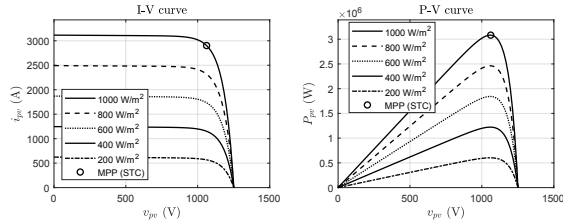

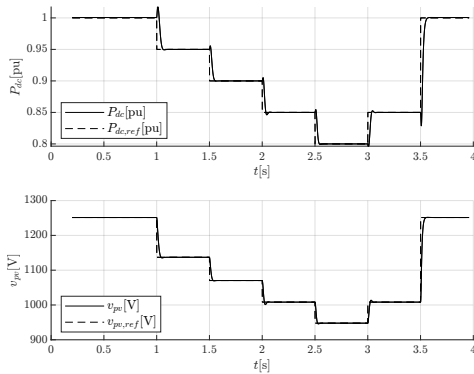Fig. 6. Primary conversion with power tracking and voltage controller

Fig. 7. Power tracking performance with decreasing and increasing power demand at constant irradiation and cell temperature

IV. MODELING AND CONTROL OF SECONDARY POWER CONVERSION UNIT

A. Reduced-order Voltage-Source Converter model

For further investigations, the following simplifications are defined: First, we assume that the terminal voltage of the voltage-source converter (VSC) has only a fundamental frequency based on a balanced three-phase system. The harmonics due to the switching semiconductors are not taken into account. Second, only symmetrical faults in the lines are treated to preserve a balanced three-phase system. Third, the line filter (LCL) is simplified to a resulting longitudinal impedance. That allows to aggregate the filter and transformer impedances (see Figure 1 and 2) to

$$L_{ft} = L_{f,1} + L_{f,2} + L_t ,\qquad(18)$$

where L_t denotes transformer impedance and $L_{f,1}$, $L_{f,2}$ the LCL filter impedance. The influence of the LCL filter capacitor C_f on the grid stability can be neglected for most issues [13]. Especially if only the fundamental frequency is examined without harmonics [16]. Fourth, the power losses of the semiconductor switches, in the magnetic components of the LCL filter and the transformer, and of the internal lines are concentrated in one linear loss function proportional to the current. Fifth, in the case of significant grid disturbance events, the VSC must react with an adequate fault current contribution (if hardware limits allow) as protection systems require. This fault ride-through (FRT) capability is only considered for the symmetrical fault case, so asymmetric faults are not considered. Based on all five assumptions, an equivalent circuit of the VSC under consideration is obtained, shown in Figure 8. The corresponding mathematical VSC model related to the equivalent circuit is given

$$-\mathbf{e}_{abc} + L_{ft}\frac{d\mathbf{i}_{abc}}{dt} + \mathbf{v}_{abc} = \mathbf{0} ,\qquad(19)$$

that describes the voltage/current dynamics with three balanced phases with $\mathbf{v}_{abc}$ and $\mathbf{i}_{abc}$. The VSC model is transformed into the time-dependent rotating dq-reference frame $\mathbf{x}_{abc} = \tilde{\mathbf{T}}_{dq}^T(\theta)\mathbf{x}_{dq}$ using the Park-Clarke matrix $\tilde{\mathbf{T}}_{dq}$, where the rotation angle is set to

$$\theta(t) \overset{!}{=} \omega t \qquad(20)$$

with the grid frequency ω at the PCC. From that follows the reduced state space model of the VSC represented in the dq-reference frame rotating with $\theta = \omega t$ (synchronize condition)

$$\dot{\mathbf{x}} = \begin{pmatrix} 0 & \omega \\ -\omega & 0 \end{pmatrix}\mathbf{x} + \frac{1}{L_{ft}}\mathbf{e} - \frac{1}{L_{ft}}\mathbf{v} \qquad(21)$$

with

$$\mathbf{x} = \begin{pmatrix} i_d \\ i_q \end{pmatrix} , \quad \mathbf{v} = \begin{pmatrix} v_d \\ v_q \end{pmatrix} , \quad \mathbf{e} = \begin{pmatrix} e_d \\ e_q \end{pmatrix} ,$$

where $\mathbf{x}$ denotes the state vector, $\mathbf{e}$ is the controllable input from the VSC and $\mathbf{v}$ denotes the voltage at the PCC as an uncontrollable input vector.

B. Cascaded grid-forming (GFOM) control scheme with inner-loop current control

The proposed controller of the grid-forming converter contains an inner loop dq current and an outer loop PQ power controller, illustrated in Figure 8. The power controller does not set the voltage directly, as most GFOL regulators usually do. Instead, the desired instantaneous voltage vector is adjusted via the current control. The reference current for

the internal controller is calculated via the voltage difference between the measurable PCC voltage and the desired voltage $\mathbf{e}_{abc}$ to be set and the VSC impedance L_{ft}.
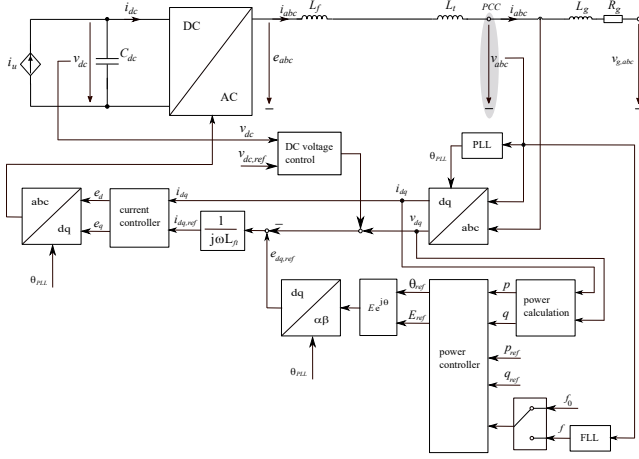

Fig. 8. Grid-forming VSC scheme with inner-loop current controller

C. Grid-forming (GFOM) control laws for power and current control

The control law of the power controller in Figure 8 is given as

$$
\begin{aligned}
\theta_u &= 2\pi \int_0^t \left(k_{I,p}\, e_{p,f}(\tau) + f_0 \right) d\tau + k_{p,p}\, e_{p,f}\,, \\
E_u &= k_{I,q} \int_0^t e_{q,f}\, d\tau + k_{p,q}\, e_{q,f} + |\mathbf{v}_{\alpha\beta}|\,,
\end{aligned}
\tag{22}
$$

where $|\mathbf{v}_{\alpha\beta}| = \sqrt{v_\alpha^2 + v_\beta^2}$ using the amplitude invariant Clarke transform $\mathbf{v}_{\alpha\beta} = \tilde{\mathbf{T}}_{\alpha\beta}\,\mathbf{v}_{abc}$ with

$$
\begin{pmatrix} v_\alpha \\ v_\beta \end{pmatrix} = \frac{2}{3}\underbrace{\begin{pmatrix} 1 & -\frac{1}{2} & -\frac{1}{2} \\ 0 & \frac{\sqrt{3}}{2} & -\frac{\sqrt{3}}{2} \end{pmatrix}}_{\tilde{\mathbf{T}}_{\alpha\beta}} \begin{pmatrix} v_a \\ v_b \\ v_c \end{pmatrix} = \sqrt{2}V \begin{pmatrix} \cos(\omega t + \phi) \\ \sin(\omega t + \phi) \\ 0 \end{pmatrix}
$$

and the filtered control error signals of the active and reactive power

$$
\begin{aligned}
\dot{e}_{pf} &= -\frac{1}{\tau_{pf}} e_{pf} + \frac{1}{\tau_{pf}} \underbrace{(p_{3\phi,ref} - p_{3\phi})}_{e_p}\,, \\
\dot{e}_{qf} &= -\frac{1}{\tau_{qf}} e_{qf} + \frac{1}{\tau_{qf}} \underbrace{(q_{3\phi,ref} - q_{3\phi})}_{e_q}\,.
\end{aligned}
\tag{23}
$$

The instantaneous active power $p_{3\phi}$ and reactive $q_{3\phi}$ are calculated by

$$
\begin{pmatrix} p_{3\phi} \\ q_{3\phi} \end{pmatrix} = \begin{pmatrix} v_\alpha & v_\beta \\ v_\beta & -v_\alpha \end{pmatrix} \begin{pmatrix} i_\alpha \\ i_\beta \end{pmatrix}.
\tag{24}
$$

using the measurements v_{abc} and i_{abc} transformed with

$$
\mathbf{i}_{\alpha\beta} = \tilde{\mathbf{T}}_{\alpha\beta}\,\mathbf{i}_{abc}\,, \qquad \mathbf{v}_{\alpha\beta} = \tilde{\mathbf{T}}_{\alpha\beta}\,\mathbf{v}_{abc}\,.
\tag{25}
$$

The signal processing of the power error signal follows the procedure

$$
\begin{aligned}
\dot{e}_{pf} &= -\frac{1}{\tau_{pf}} e_{pf} + \frac{1}{\tau_{pf}} (p_{3\phi,ref} - v_d\, i_d - v_q\, i_q)\,, \\
\dot{e}_{qf} &= -\frac{1}{\tau_{qf}} e_{qf} + \frac{1}{\tau_{qf}} (q_{3\phi,ref} - v_q\, i_d + v_d\, i_q)\,, \\
\dot{x}_{I,p} &= e_{pf}\,, \\
\dot{x}_{I,q} &= e_{qf}\,.
\end{aligned}
\tag{26}
$$

To ensure that the inverter is operated within the nominal current range, a current controller (see Figure 8) is underlying the grid-forming operation.

$$
\begin{aligned}
e_d &= \underbrace{v_d - \omega L_{ft}\, i_q}_{\text{decoupling term}} + k_{p,i_d}(i_{d,ref} - i_d) + k_{I,i_d} \int_0^t (i_{d,ref} - i_d)\, d\tau\,, \\
e_q &= \underbrace{v_q + \omega L_{ft}\, i_q}_{\text{decoupling term}} + k_{p,i_q}(i_{q,ref} - i_q) + k_{I,i_q} \int_0^t (i_{q,ref} - i_q)\, d\tau\,.
\end{aligned}
\tag{27}
$$

with the current setpoints calculated by

$$
i_{q,ref} = -\frac{1}{\omega L_{ft}}(e_{d,ref} - v_d)\,, \quad i_{d,ref} = \frac{1}{\omega L_{ft}}(e_{q,ref} - v_q)\,.
$$

V. SIMULATION RESULTS FOR DIFFERENT TEST SCENARIOS

Finally, in this section, the primary power conversion with the secondary power conversion part will now be combined as shown in Figure 2. For a reliable analysis, relevant scenarios based on grid events, volatile regenerative resources and load changes are applied. The test scenarios are designed to cover various functionalities occurring if PV power plants participate in a bulk power system. The focus is on studying the system's response to active and reactive power demands, as well as responses to the change in voltage magnitude or phase jumps. The latter is used to emulate certain grid events, such as line tripping and voltage drop due to short circuits in the line. Furthermore, system responses from sudden changes in available primary energy sources are also to be analyzed.

A. Response to Active Power Request

The active power demand is increased by a step of 0.1 per unit. Regarding the PV systems without energy storage, this active power command can only be achieved if the current primary energy source provides sufficient power. For this reason, the RES power plant is operated in a derating operation, where the PV generator operates at a lower power than it could deliver based on renewable energy conditions. The simulation results are shown in Figure 10 and Figure 11. To benchmark the performance of the GFOM converter, simulations with a conventional Grid Following converter are also presented. One can see well how the reference value for the PV voltage in the diagram v_{pv} over t is adjusted within $10\,\text{ms}$. The relatively fast change of the power fed into the DC link leads to some oscillations in the active power that decay after $300\,\text{ms}$.

B. RES fluctuation: Irradiation step

In this scenario, the power of the primary source decreases. In absolute terms, the initial setting starts with the nominal value at standard test conditions, which is then lowered by 20% for $t \geq t_e = 0.01\,\text{s}$. After a negative jump in the primary source, the power supplied by the irradiation is no longer sufficient to provide the desired active power at the PCC. This leads to a steady-state offset where only approximately 73% power instead of 80% is generated. The simulations results are shown in Figure 10 and Figure 11.
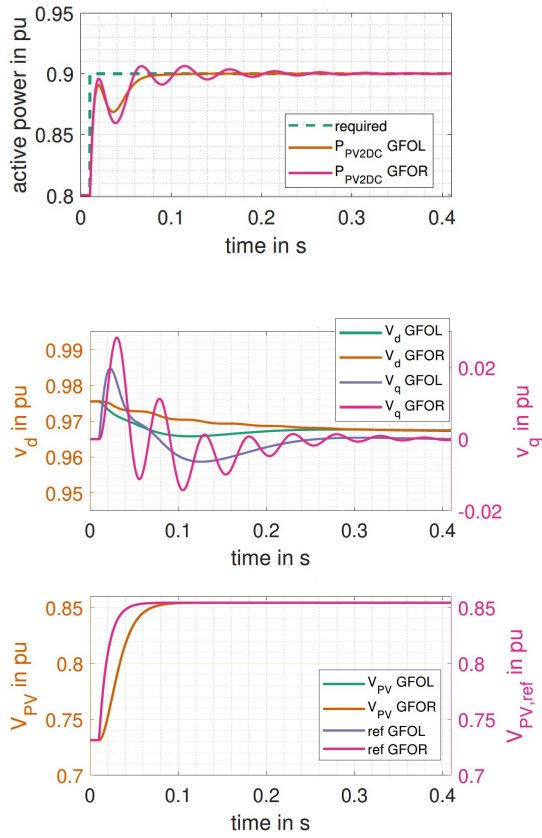
Fig. 9.   System response of active power request at $t = 0.01\,\mathrm{s}$

C. Response to Reactive Power Request

In this test case only the reactive power is adjusted. The active power demand is kept constant, which means that the power generation of the PV-generator remains constant. The reactive power demand varies step-wise by 0.3 pu. This process is mainly governed by the secondary conversion side, where either the current setpoint is recalculated, or the exciter of the synchronous generator is used to provide the desired level of reactive power. A variation of reactive power directly acts on the voltage magnitude of the considered connection point within the electrical grid, thus enhancing voltage stabilization. The changes following a reactive power demand step are governed by the outer loop power control acting on the current set point of the VSC.

In both VSC control concepts, the course of reactive power depends on the selected control parameters. As a result of the reactive power
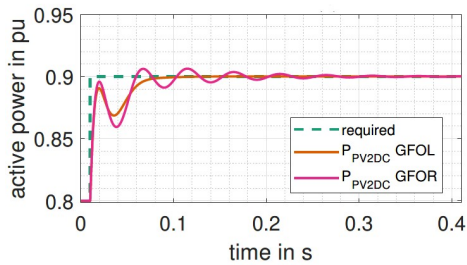

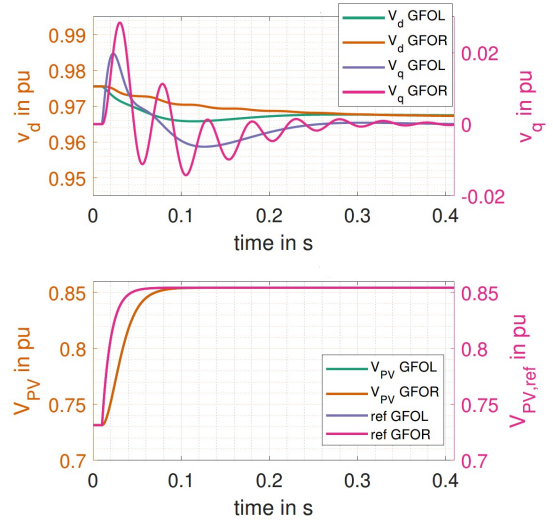Fig. 10.   System response of the injected active power after irradiation step at $t_e = 0.01\,\mathrm{s}$

Fig. 11.   System response after irradiation step at $t_e = 0.01\,\mathrm{s}$

injection, the voltage at the PCC is raised from 0.97 pu to 1.07 pu, as shown in Figure 6.6. The transient in PCC voltage results in a slight excitation of the PLL frequency, which decays without oscillation in the range of milliseconds. This has no influence on the estimation of the power frequency by the PLL, which remains undisturbed. The cascaded power and current controllers in the inverter adjust the inverter terminal voltage to force the desired reactive power injection.
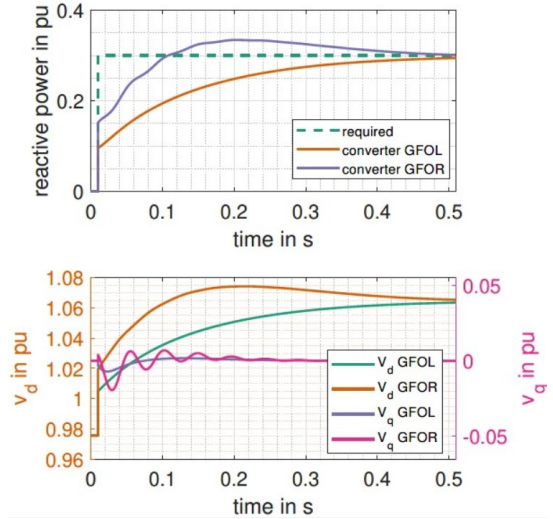

Fig. 12.   Response after step change of reactive power request at $t_e = 0.01\,\mathrm{s}$

D. Grid Disturbance Rejection

In this test case, a voltage magnitude drop to 0.9 pu symmetrically at all three phases is performed:

$$V_g = \begin{cases} 1.0V_B & t < t_e \\ 0.9V_B & t \geq t_e \end{cases}, \qquad (28)$$

where V_B denotes the base voltage. The drop level is chosen to evaluate the initial disturbance rejection dynamics in normal

operation, i.e., without reaching limitations or activating a fault mode due to an identified under-voltage. This relates to small-signal stability. The transfer to a new operating point, which leads back to the feed-in of the power before the event, is performed by the cascaded controller in the voltage source converter. The effect of the voltage drop on the VSC active and reactive power injection at the PCC is illustrated in Figure 13 and Figure 14. The step-wise change of the grid voltage magnitude reduces the voltage at the PCC as shown by $v_{d,q}$ in Figure 15.
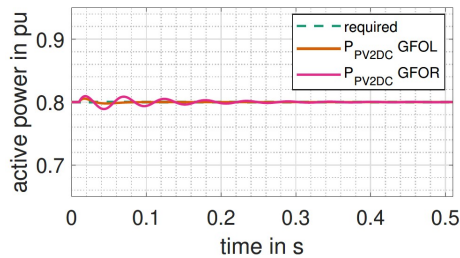

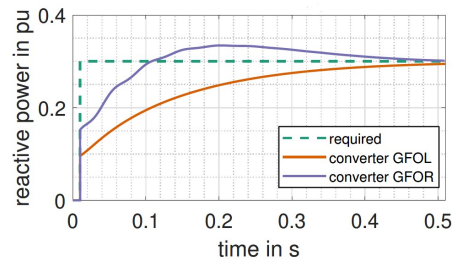Fig. 13. System response of injected active power at PCC after voltage magnitude drop at $t_e = 0.01\,\mathrm{s}$

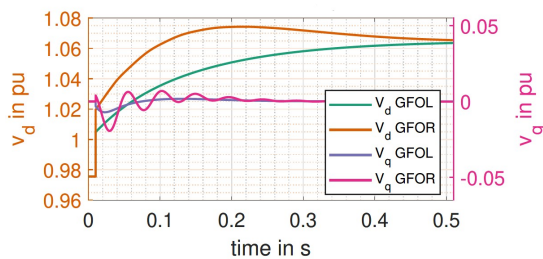Fig. 14. System response of injected reactive power at PCC after voltage magnitude drop at $t_e = 0.01\,\mathrm{s}$

Fig. 15. Voltage $v_{d,q}$ step response in the grid-forming (GFOM) and grid-following (GFOL) converter after voltage magnitude drop at $t_e = 0.01\,\mathrm{s}$

VI. Conclusion

A photovoltaic power plant with decentralized control of the primary and secondary power conversion was presented. The contribution of the paper consists of a holistic presentation of an overall plant with a novel demanded power tracking scheme of the photovoltaic generator (primary conversion) and the converter-interfaced generation (secondary conversion) by cascaded controlled GFOM or GFOL converter connected to an equivalent grid. The decentralized controllers were designed based on reduced first-principles models, where the control loops were explained in detail. The dynamic behavior was investigated using large-signal events. In future work, the single-machine scenario will be extended to multi-machine scenarios subjected to the same test scenarios for a more realistic stability analysis.

References

[1] S. Kusche, F. Pöschke, and H. Schulte, "POwering SYstem flexibiliTY in the Future through RES (POSYTYF), Deliverable 2.2 - Report on Objectives and Assessment Criteria for Controller Design," HTW Berlin, Tech. Rep., 2022. [Online]. Available: https://posytyf-h2020.eu/english-version/deliverables

[2] H. Schulte and S. Kusche, "Fast power tracking control of PV power plants for frequency support," *at - Automatisierungstechnik*, vol. 71, no. 10, pp. 891–908, 2023. [Online]. Available: https://doi.org/10.1515/auto-2023-0029

[3] C. Messasma, A. Barakat, S. E. Chouaba, and B. Sari, "PV system frequency regulation employing a new power reserve control approach and a hybrid inertial response," *Electric Power Systems Research*, vol. 223, p. 109556, 2023.

[4] C. Messasma, S. E. Chouaba, B. Sari, and A. Barakat, "An approach for Power Reserve Control (PRC) Strategy Based on a Novel ANN Model," in *Advanced Computational Techniques for Renewable Energy Systems*, M. Hatti, Ed. Cham: Springer International Publishing, 2023, pp. 594–601.

[5] R. Kumar, B. Sahu, C. K. Shiva, and B. Rajender, "A control topology for frequency regulation capability in a grid integrated PV system," *Archives of Electrical Engineering*, vol. vol. 69, no. No 2, pp. 389–401, 2020.

[6] P. Zarina, S. Mishra, and P. Sekhar, "Exploring frequency control capability of a PV system in a hybrid PV-rotating machine-without storage system," *International Journal of Electrical Power & Energy Systems*, vol. 60, pp. 258–267, 2014.

[7] M. Ahmed, I. Harbi, R. Kennel, J. Rodriguez, and M. Abdelrahem, "Model-Based Maximum Power Point Tracking Algorithm With Constant Power Generation Capability and Fast DC-Link Dynamics for Two-Stage PV Systems," *IEEE Access*, vol. 10, pp. 48 551–48 568, 2022.

[8] B. Weise, A. Korai, and A. Constantin, "Comparison of Selected Grid-Forming Converter Control Strategies for Use in Power Electronic Dominated Power Systems," in *Proceedings of the 18th Wind Integration Workshop*, Dublin. Ireland, October 2019.

[9] NN, "Grid Forming Technology, Bulk Power System Reliability Considerations," Nerc, North American Electric Reliability Corporation, 3353 Peachtree Road NE, Suite 600, North Tower, Atlanta, GA 30326, Tech. Rep., 2021.

[10] H.-P. Beck and R. Hesse, "Virtual synchronous machine," in *2007 9th International Conference on Electrical Power Quality and Utilisation*, 2007, pp. 1–6.

[11] Q.-C. Zhong, W.-L. Ming, and Y. Zeng, "Self-synchronized universal droop controller," *IEEE Access*, vol. 4, pp. 7145–7153, 2016.

[12] I. Erlich, A. Korai, and F. Shewarega, "Study on the minimum share of conventional generation units required for stable operation of future converter-dominated grids," in *2018 IEEE Power & Energy Society General Meeting (PESGM)*, 2018, pp. 1–5.

[13] N. Klaes, N. Goldschmidt, and J. Fortmann, "Voltage Fed Control of Distributed Power Generation Inverters with Inherent Service to Grid Stability," *Energies*, vol. 13, no. 10, 2020. [Online]. Available: https://www.mdpi.com/1996-1073/13/10/2579

[14] T. Qoria, E. Rokrok, A. Bruyere, B. François, and X. Guillaud, "A PLL-Free Grid-Forming Control With Decoupled Functionalities for High-Power Transmission System Applications," *IEEE Access*, vol. 8, pp. 197 363–197 378, 2020.

[15] I. Subotić and D. Groß, "Power-Balancing Dual-Port Grid-Forming Power Converter Control for Renewable Integration and Hybrid AC/DC Power Systems," *IEEE Transactions on Control of Network Systems*, vol. 9, no. 4, pp. 1949–1961, 2022.

[16] R. Teodorescu, M. Liserre, and P. Rodríguez, *Grid Converters for Photovoltaic and Wind Power Systems*. John Wiley & Sons, Ltd., 2011.

[17] Z. Lendek, T. M. Guerra, R. Babuška, and B. de Schutter, *Stability Analysis and Nonlinear Observer Design Using Takagi-Sugeno Fuzzy Models*, ser. Studies in Fuzziness and Soft Computing. Berlin, Heidelberg: Springer Berlin Heidelberg, 2011, vol. 262.

[18] M. Chilali, P. Gahinet, and P. Apkarian, "Robust pole placement in lmi regions," *IEEE Transactions on Automatic Control*, vol. 44, no. 12, pp. 2257–2270, 1999.

[19] P. Gahinet, A. Nemirovskii, A. J. Laub, and M. Chilali, Eds., *The LMI Control Toolbox*, Lake Buena Vista, USA, 1994.